Version of Record: https://www.sciencedirect.com/science/article/pii/S0168900220303284
Manuscript_48e886b8c4784c30faa240c4b9d405a8

Fluid-dynamics and transport of ^{210}Po in the scintillator Borexino detector: a numerical analysis

Authors and affiliations:

V. Di Marcello[1,*], D. Bravo-Berguño[2,i], R. Mereu[3], F. Calaprice[4], A. Di Giacinto[1], A. Di Ludovico[4], Aldo Ianni[1], Andrea Ianni[4], N. Rossi[1], L. Pietrofaccia[4]

[1]INFN Laboratori Nazionali del Gran Sasso, 67010 Assergi (AQ), Italy

[2]Università degli Studi e INFN, Dipartimento di Fisica, 20133 Milano, Italy

[3]Politecnico di Milano, Energy Department, 20156 Milano (MI), Italy

[4]Princeton University, Physics Department, Princeton, NJ 08544, USA

*corresponding author (valentino.dimarcello@lngs.infn.it)

phone: +39 0862 437360

[i] Present address: Universidad Autónoma de Madrid, Ciudad Universitaria de Cantoblanco, 28049 Madrid, Spain

Abstract:

Moving beyond the important contributions to neutrino physics obtained by the Borexino experiment during the last years, research activities are ongoing at INFN Gran Sasso National Laboratories to further improve the detector sensitivity in order to perform an accurate measurement of the subdominant CNO solar neutrino rate. To this purpose, the improvement of the detector fluid-dynamic stability is the key to further reduce the ^{210}Po background, that is continuously being transported inside the measurement fiducial volume by convective currents. In this framework, numerical simulations of the detector fluid-dynamics may help to better comprehend the ^{210}Po behaviour, and also to suggest effective countermeasures, able to minimize the natural convection inside the detector.

In the present work, two-dimensional numerical simulations have been performed to improve the current understanding of Borexino thermal and fluid-dynamics. Adopted models have been optimized for different regions and periods of interest, focusing on the most critical aspects that were identified as influencing the polonium background concentrations. In particular, a Borexino-specific benchmark was constructed in order to validate the model temperature predictions. The derived inner vessel surface temperatures are successively used as boundary conditions for a more refined convective model of the inner most part of the detector. Based on the calculated convective currents, the transport behaviour of background ^{210}Po inside the detector active volume was investigated by means of a convection-diffusion model, showing a reasonable good agreement between calculations and experimental data.

Keywords:

Neutrino detector; Computational Fluid Dynamics; ^{210}Po Background; Transport analysis; Natural convection

1. Introduction

The main objective of the Borexino liquid scintillator neutrino detector is the high-precision determination of neutrino fluxes in the low energy (sub-MeV) region of the solar neutrino spectrum. Borexino has obtained unprecedented results in determining all major solar neutrino components during its 10 years of operation [1]: direct detections of pp [2], pep [3] and ^{7}Be [4] neutrinos; and lowest-threshold observation of ^{8}B [5] at 3 MeV, as well as the best available limit in the CNO solar flux [4]. Recently, the collaboration has succeeded in performing a comprehensive, wideband simultaneous determination of all the components previously measured individually, furthermore with improved precision in each of them (10% accuracy for pp, 5σ evidence for pep, 2.7% accuracy for ^{7}Be and < 8.1 cpd/100t[1] for CNO), through the analysis of post-scintillator-purification data [1]. In addition, Borexino is able to measure the flux of geoneutrinos with high precision ([6] and recently updated [7]), thanks to the extremely clean electron antineutrino ($\bar{\upsilon}_e$) channel. The unique and extremely radio-pure conditions reached in the Fiducial Volume (FV) of the detector (with values $\leq 10^{-19}$ g/g for ^{238}U and ^{232}Th [1]), accomplished thanks to a combination of ultra-clean construction and fluid-handling techniques, as well as dedicated scintillator purification campaigns [8] and internal calibration [9], made these achievements possible.

About two years after the purification campaign carried out in 2011, the ^{210}Po background was still significantly high, but low enough to appreciate the out-of-equilibrium correlation with temperature upsets, suggesting the need of increasing the detector thermal stability in order to avoid undesired background fluctuations due to the mixing of the scintillating fluid inside the inner vessel of the detector. Significant improvements to the stability of Borexino's internal fluid-dynamics were achieved starting mid-2015 thanks to the installation of the Thermal Insulation System (TIS): a 20 cm-thick insulating mineral-wool (Ultimate Tech Roll 2.0 – Isover [10]) layer on the outer surface of the detector to minimize the effect of environmental temperature variations, as well as the implementation of an Active Temperature Control System (ATCS) located at the dome of the water tank of Borexino [11]. This resulted in a further background reduction, but ^{210}Po is still showing an asymmetric profile different between top and bottom of the FV as well as an oscillating, seasonally-influenced, behaviour. The favoured hypothesis is that extremely dilute, but measurable concentrations of background radioisotopes

[1] counts / (day · 100 tonnes)

migrates from the ultraclean, but relatively more contaminated, surface of the inner vessel towards the interior of the virtual, software-defined FV (where physics data is selected). This would directly correlate fluid dynamics with background migration, which is only attenuated through the corresponding isotopes decay half-lives.

A monitoring Latitudinal Temperature Probe System (LTPS) was also installed in 2015 as an early attempt to better understand and constrain uncertainties on the detector thermal profile. Several temperature probes were added in different Borexino locations, which significantly improved the temperature measurements compared to the old legacy probes. Preliminary Computational Fluid Dynamics (CFD) studies were also carried out [11].

In this paper, we have further extended the numerical analysis by improving the two-dimensional model accuracy as well as the validation framework. In addition, a simplified transport model was developed, aiming at simulating the ^{210}Po migration inside the inner vessel for selected periods of the Borexino lifetime.

In particular, section 2 of this paper will give a brief description of the Borexino experiment. Section 3 will deal with the correlation existent between background stability and detector thermal conditions. Section 4 will describe on the Computational Fluid Dynamics (CFD) models developed in order to more comprehensively understand the detector past and future thermal behaviour, along with the numerical settings. Section 5 will detail with the validation of the thermal transport prediction capabilities of the CFD model. Section 6 will focus on the inner detector refined CFD model aimed at providing an insight into the fluid movement inside this closed, stratified, near-equilibrium system. Section 7 will describe the results of the simplified transport model and the comparison with the measured polonium profiles.

2. The Borexino experiment

Borexino is located in the underground facilities (3,800 m water-equivalent) Hall C of the Gran Sasso National Laboratories (LNGS). The detector can perform real-time measurements of solar neutrinos interacting with about 300-tonne target of ultrapure organic liquid scintillator, consisting of pseudocumene (1,2,4-trimethylbenzene, PC) solvent with 1.5 g/l of 2,5-diphenyloxazole (PPO) scintillating solute, that is contained inside a 125 μm thick transparent spherical nylon inner vessel (IV) of 8.5 m diameter. Solar neutrinos are mainly detected by measuring the energy and position of electrons scattered by neutrino-electron elastic interactions. Borexino has an energy resolution of 5% at 1 MeV, and a spatial resolution of the order of 10 cm for background events considered in the FV. The scintillator promptly converts the kinetic energy of electrons by emitting photons, which are detected and converted into electronic signals (photoelectrons) by about 2200 photomultipliers tubes (PMTs) installed on a concentric 13.7 m-diameter Stainless Steel Sphere (SSS, see Figure 1).

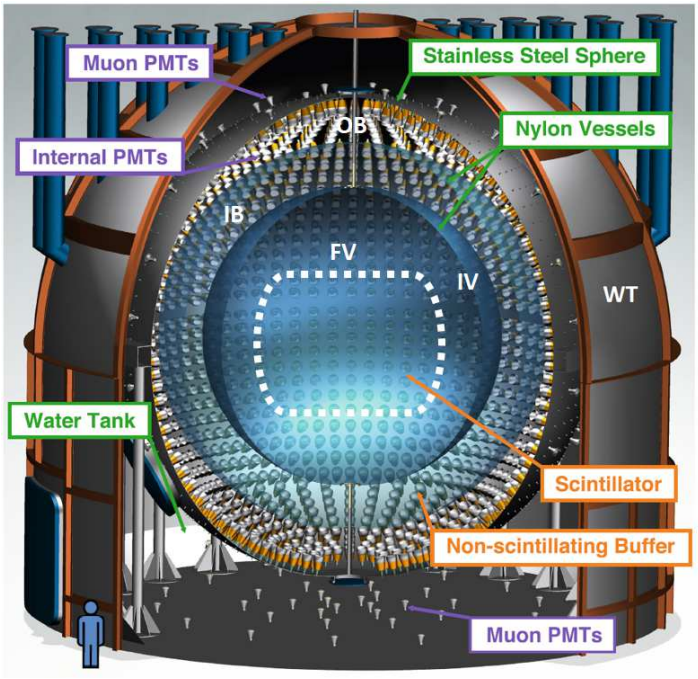

Figure 1: Schematic view of the Borexino detector.

The buffer region located between the inner vessel and the SSS serves as a radiation shield for external gamma rays and neutrons and consists in 889 tonnes of ultra pure, non-scintillating fluid divided into two smaller concentric volumes by a second nylon sphere: the outer buffer (OB) and the inner buffer

(IB). Finally, the SSS is immersed in a 2100-tonne Water Tank (WT) acting as a Cherenkov detector tagging residual cosmic muons.

Borexino is still today the most sensitive neutrino detector in the world with a record low scintillator contamination of $\leq 10^{-19}$ g/g achieved for ^{238}U and ^{232}Th. Nevertheless, ongoing efforts to achieve the first measurement of the CNO solar neutrino component (≤ 1% of the Sun output [12]) necessitate further background reduction, since the recoil spectral shape of CNO neutrinos is almost completely correlated with that of ^{210}Bi[2]. This is an intrinsic Borexino background whose spectral contribution is close to the sought signal, lying in the 400 p.e. energy window, where the CNO rate is expected to be higher than that from the ^{7}Be and pep neutrinos (see Figure 2), and its ß-decay signal is only statistically-discernible from neutrino scattering interactions.

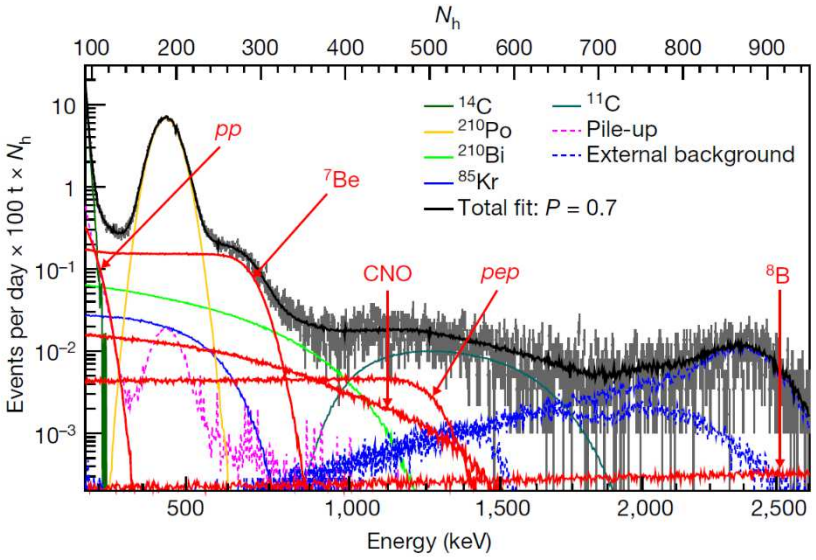

Figure 2: Borexino spectrum in the main analysis energy range and corresponding fits for neutrino and backgrounds components. The horizontal upper scale is (N_h) is the total number of photons collected for each event.

An accurate independent determination of the ^{210}Bi concentration is essential to perform the statistical discrimination. In particular, a precision level in excess of 10-15% is required for a long enough period of time, in order to simultaneously determine the very low expected CNO neutrino counts of 3.6-5 cpd/100t (value depending on the solar metallicity models) [1]. This can only be achieved through the measurement of ^{210}Bi decay daughter ^{210}Po (see decay chain in Eq. (1) with the corresponding half-lives),

[2] For the sake of completeness, also ^{85}Kr is actually correlated in a spectral fit of the species (see Figure 2), but it can be constrained independently and is not an issue in the energy window 0.75-1 MeV, where CNO neutrinos should dominate the signal.

because the signal deriving from the β decay of bismuth produces an indistinguishable signal to CNO [13]. Therefore, the strategy is to obtain at least within the FV, a ^{210}Po level that has asymptotically reached a plateau corresponding to the secular equilibrium levels of ^{210}Bi, ensuring out-of-equilibrium components have decayed away (initial rate after 2012 purifications was ~800 times higher than that of bismuth).

$$^{210}_{82}\mathrm{Pb} \xrightarrow[22.3\ \mathrm{y}]{\beta^-} {}^{210}_{83}\mathrm{Bi} \xrightarrow[5\ \mathrm{d}]{\beta^-} {}^{210}_{84}\mathrm{Po} \xrightarrow[138.4\ \mathrm{d}]{\alpha} {}^{206}_{82}\mathrm{Pb}_{(\mathrm{stable})} \quad (1)$$

This condition is extremely difficult to obtain, even though the polonium background has significantly decreased during the past few years as shown in Figure 3. In fact, significant fluctuations in the ^{210}Po levels have prevented reaching an ideal stabilization. The reason is the presence of convective currents in the liquid scintillator which are continuously providing a source of ^{210}Po migrating inside the FV from the surface of the IV, which is known to have higher concentration of ^{210}Pb.

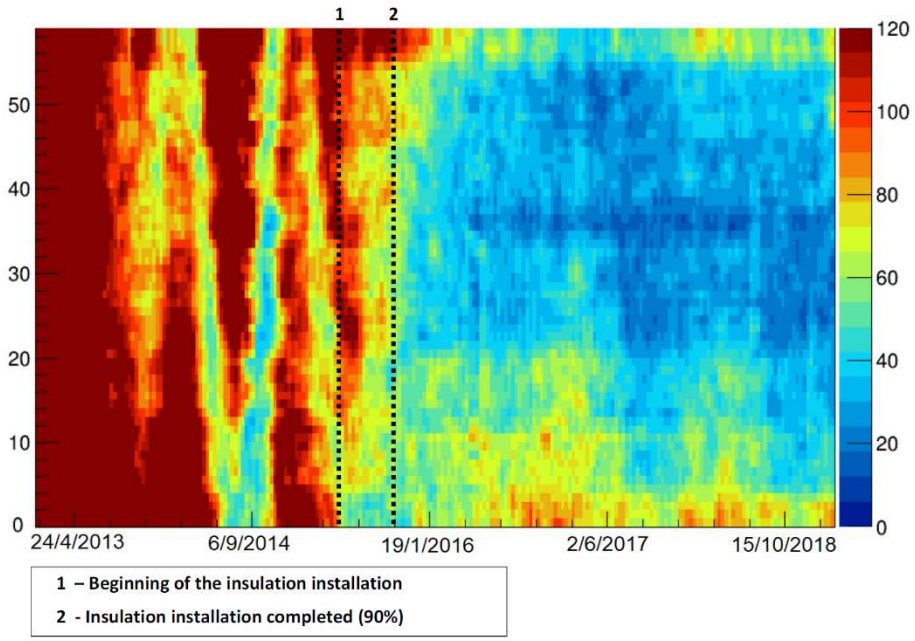

Figure 3: Regional map of polonium concentrations with respect to time (color code: cpd/100t). The y axis indicates regional subdivisions of a 3m-radius FV, running from its bottom to its top.

3. Thermal behaviour and background stability

The typical temperature profile of Borexino exhibits a stable thermal stratification characterized by a temperature gradient that increases monotonically with height. Denser isotherms are present in the bottom half, indicating a sharper gradient in that region, that then smooths out toward the top, where temperatures are more uniform. Heat is exchanged with the rock, steel and concrete at the bottom, as well as with the air surrounding the WT, and ideally should contribute to keeping that gradient profile. In real conditions though, local temperature inhomogeneities in the ambient air as well as seasonal upsets, deviate the thermal profile from this ideal situation, and generate spatial and temporal perturbations. For this reason, the LTPS was conceived as a vertical profile monitoring system, with several sensors located on the north and south side of Borexino for technical reasons, as shown in Figure 4. In particular, the system consists of 28 internal probes inserted into 14 ports of the SSS through PVC tubes, which were previously foreseen for the insertion of calibration sources. Across each port, there are 2 sensors separated by about 1m, so that the one at the end of the PVC tube is inside the outer buffer (Re-entrant Buffer – ReB) while the other sensor is in the water tank (Re-entrant Water – ReW), with the SSS half a meter between both. Moreover, 20 additional sensors (the WT probes) are installed on the water tank surface, complemented by 6 probes located in a T-shaped service tunnel under the detector (Icarus pit).

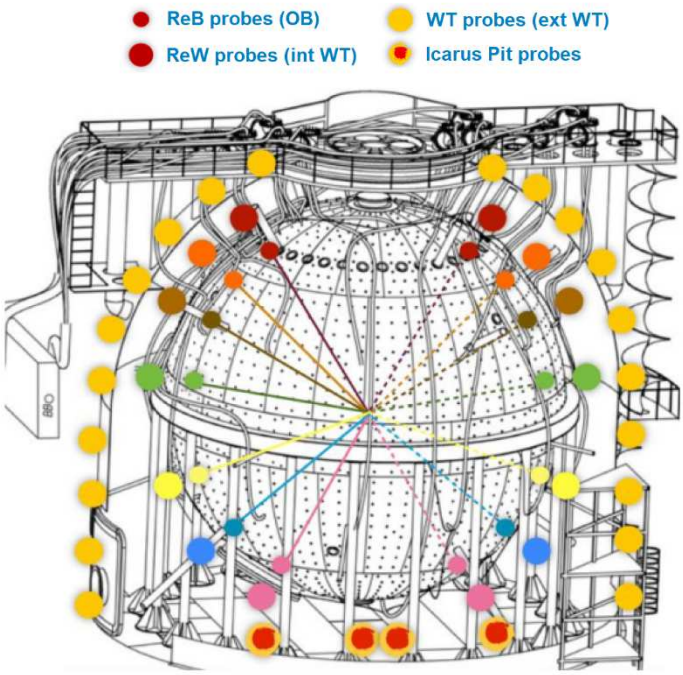

Figure 4: Borexino detector sensors positioning.

ReW, ReB and WT sensors technical specifications are briefly reported in Table 1, whereas the reader can refer to [11] for the details concerning the data acquisition (DAQ) software, and the calibrations procedures. In addition to the relatively new temperature monitoring system, Borexino has further probes for exterior ambient air and WT surface readings.

Specification	Value
Temp. transducer model	TPL-BTA AD590JH
Cable length	30 m
Maximum diameter	7 mm
Range	-50°C / +150°C
Specified accuracy	±0.2°C
Specified resolution	0.07°C
Response time	8-10 s (still water) 45 s (stirred water) 100 s (moving air)

Table 1: Vernier Extra-Long Probes specifications.

The LTPS has significantly improved the understanding of Borexino's thermal behaviour, as exemplified by the determination of an upper limit constraint for the thermal transport speed across the SSS (around 1-1.2 m/day) demonstrating the extremely high thermal inertia to temperature transients [11]. Another relevant characteristic, that will be strongly highlighted in the numerical analysis section, is the presence of a thermal asymmetry - very small if compared to the vertical temperature gradient - between the north and south sides of the detector caused by the different exterior environmental conditions.

The temperature profiles are shown only in the case of the ReB probes (Figure 5) for the sake of brevity, along with the main milestones of Borexino thermal stabilization operations. Due to the significant oscillating temperature behaviour shown at the start of LTPS operations in 2014-15, it was decided to implement the TIS, whose installation started in May 2015 and reached an almost complete insulation (90% of the surface) of the detector around October 2015. Having an extremely low conductivity value of about 0.03-0.04 W/m·K, the insulation layer effectively increased the Borexino thermal resistance. Also the loop recirculation pump for the lower half of the water in the WT was shut down, in order to increase the thermal stratification, as indicated by the sudden temperature drop of the lower probes at the end of 2015. In addition, at the end of 2016 the temperature active control system installed on the dome of the detector was completed and turned on, with the aim of avoiding possible transient or long-term effects negatively affecting fluid stability, through the maximization of a positive thermal gradient

between top and bottom of the detector, as well as the minimization of external disturbances in the top and most sensitive region.

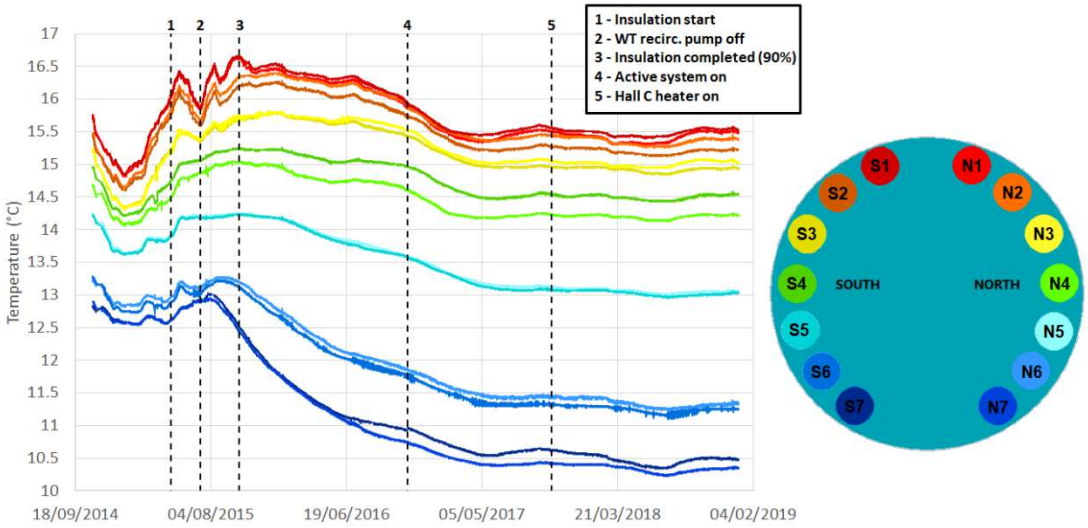

Figure 5: Borexino outer buffer temperatures (ReB) from the start of data taking (colour on-line).

The fully-insulated period showed remarkable stability in all areas of the detector, except for the foreseen bottom cooling down (in the long run, increasing stability through an increased thermal gradient). On the other hand, the insulation brought with it a decrease in top temperatures, which caused a slowdown in the increase of the gradient. The ATCS operation partially off-sets this trend, locking the top temperature at a constant value that should never be surpassed by environmental conditions.

As already discussed, the hypothesis of a continuous polonium source located at the IV surface has been further strengthened after the thermal stabilization, when the polonium activity inside the fiducial volume has shown a remarkable decrease after the temperature stabilization (Figure 3). However, the seasonal oscillation in ^{210}Po concentration between the top and the bottom of the FV, already visible since 2013, is still occurring nowadays, confirming the correlation with external temperature trends. Even if an extremely low background level was only reached at the end of 2018, the polonium concentration may still be too high for an accurate determination of the CNO rate. However, it must be mentioned that the ^{210}Bi constraint can be used in this case as an upper limit in the spectral fit, leading, even in this non-ideal condition, to an evidence of CNO.

4. CFD modelling approach

The CFD methodology developed for the study of the Borexino detector along with the different benchmarking models set-up to qualitatively understand the detector fluid-dynamics regime has been comprehensively described in [11]. However, only preliminary CFD analyses were carried out. In this study, such models have been further refined and improved concerning both the spatial discretization and the interpolation of the boundary conditions. Due to the required large number of mesh elements and the available computational resources, the 2D modelling approach is employed also in this work. The 2D approach has been validated in a previous study [11] demonstrating the capability to correctly reproduce the fluid dynamic behaviour for several benchmarks. Nevertheless, it must be mentioned that preliminary 3D calculations, recently carried out, are consistent with the bi-dimensional representation, further strengthening the validity of current approach. Concerning the validation benchmark, that consists in the verification of the model temperature predictions, the analysis has been further extended to a longer transient (about 9 months from April to December 2015), and to more recent periods (during 2018) of Borexino lifetime. In this section the governing equations, numerical geometry, discretization and the numerical modelling set-up used for this purpose are described in detail.

4.1 Governing equations

A commercial finite volume solver, ANSYS-Fluent release 19.2 [14], based on the numerical solution of the Navier-Stokes and energy transport equations for all grid cells, has been used for modelling the flow field. Mass, momentum and energy conservation equations for incompressible Newtonian fluids with constant viscosity and density in laminar flows have been used, as reported in Eqs. (2), (3) and (4), respectively:

$$\frac{\partial \rho}{\partial t} + \nabla \cdot (\rho \mathbf{u}) = 0 \tag{2}$$

$$\frac{\partial \rho \mathbf{u}}{\partial t} + \nabla \cdot (\rho \mathbf{u}\mathbf{u}) = -\nabla p + \nabla \cdot \bar{\bar{\tau}} + \bar{\rho}\mathbf{g} \tag{3}$$

$$\frac{\partial \rho E}{\partial t} + \nabla \cdot \left(\mathbf{u}(\rho E + p)\right) = \nabla \cdot \left(k\nabla T + (\bar{\bar{\tau}} \cdot \mathbf{u})\right) \tag{4}$$

where **u**, p and E are the velocity vector, static pressure and energy, respectively. ρ**g** is the gravitational body force, k the thermal conductivity and τ the stress tensor [15]. Natural convection flow is modelled by means of the Boussinesq approximation (Eq.(5)) which takes into account density variations only for the buoyancy term in the momentum equation.

$$\bar{\rho}\mathbf{g} = (\rho - \rho_0)\mathbf{g} \cong -\rho_0\beta(T - T_0)\mathbf{g} \quad (5)$$

where β is the volumetric thermal expansion coefficient and ρ_0 and T_0 are the reference values for density and temperature, respectively.

4.2 Mesh generation

The mesh generation process is in general a critical step, but it is particularly crucial for the present numerical analysis due to the large domain under consideration, characterized by very low flow intensity and the presence of natural convection. The domain is discretized with unstructured quadrilateral two-dimensional cells, coupled with a boundary layer grid along the walls. The mesh size is defined for each modelled geometry and it is based on a preliminary mesh sensitivity analysis.

Similarly to the previous study [11], two different numerical models have been developed: the *2D water ring* model (Figure 6) and the *IV sphere* model (Figure 7) which are featured by a different discretization approaches in order to avoid a higher number of elements and to reduce the related computational cost and time for the simulations. The use of two numerical domains also aims to define the boundary conditions for the inner vessel through the available experimental data of the temperature around the outer water ring. After the *2D water ring* calculation, the *IV sphere* model is adopted to more accurately predict the velocity pattern inside the detector, having a more refined mesh discretization.

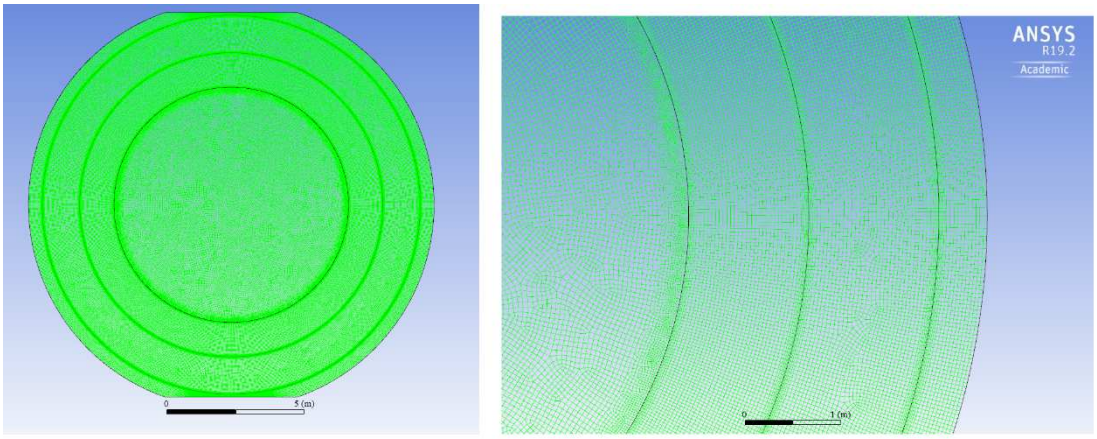

Figure 6: Sketch of the *2D water ring* model and discretization.

As far as the *2D water ring* model is concerned, the mesh is composed by approximately 118,000 quadrilateral control volumes with local refinement close to the walls and all relevant parts of the numerical domain. The cell size varies between a minimum of 8.9 mm to a maximum of 6.9 cm. On the other hand, the mesh of the *IV sphere* model is more refined consisting of approximately 530,000 control volumes with specific refinements near the walls to take into account the viscous and thermal boundary layer. In this case, cells have a minimum and maximum size of 5 mm and 1.6 cm, respectively. Domains and related grids are reported in Figure 6 and Figure 7, with a view of the local refinements. The approach used for determining the boundary conditions is described more in detail in Section 4.5.

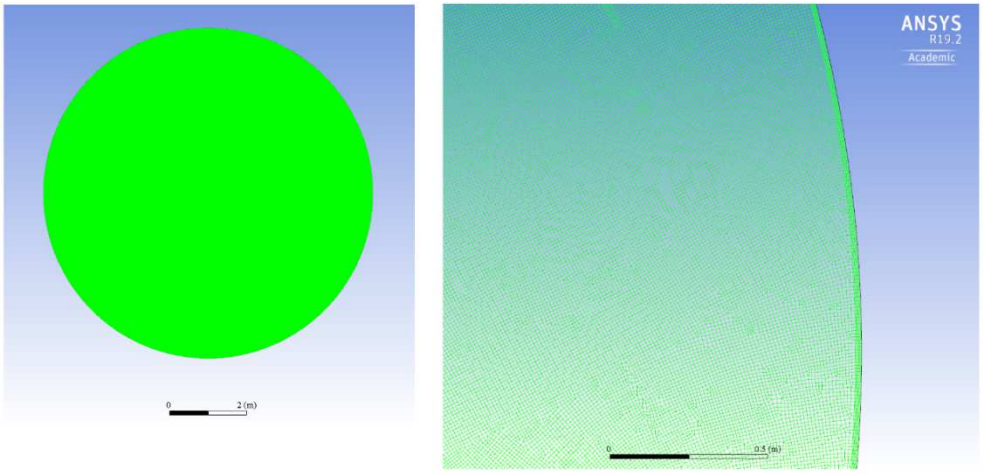

Figure 7: Sketch of the Inner vessel *IV Sphere* model with particular of the mesh.

4.3 Numerical modelling

The solution algorithm chosen in ANSYS-Fluent to solve the set of equations is the pressure-based 'segregated solver', that treats the governing equations in a sequential way. Due to the strong non-linear coupling, several iterations of the solution loop must be performed before a converged solution is obtained. The transient simulation solver is based on the coupling pressure-velocity PISO algorithm [15], that is able to guarantee the convergence especially for relatively larger time step compared to other algorithms. The time step size is defined conservatively, based on the natural convection time constant constraint [15], leading to a value of 9 s and 4.5 s for the *2D water ring* and the *IV sphere* models, respectively. As far as the discretization schemes are concerned, the configuration reported in Table 2 is adopted for all the calculations.

Term	Scheme
Transient	First Order Implicit
Gradient	Least Squares Cell Based
Pressure	Body Force Weighted
Momentum, Energy	Third-Order MUSCL

Table 2: numerical schemes

4.4 Thermal and physical properties

The main properties of the Borexino liquid scintillator, described here below, refer to pure pseudocumene, since the mixture differences (PC + DMP in the buffer and PC + PPO in the IV) are substantially negligible for the purpose of the present paper.

1. PC density is specified at the operating temperature of 288K and it is equal to 881 kg/m^3 [16].
2. Heat capacity (c_P) is given by a correlation taking into account the temperature dependency, based on data reported in [17]. The derived polynomial function is shown in Eq. (6):

$$c_P = 1497.08 - 1.1442 \cdot T + 7.13 \cdot 10^{-2} \cdot T^2 \quad (6)$$

3. Thermal conductivity is prescribed by the correlation reported in Eq. (7) [18]:

$$k = 0.203 - 2.72 \cdot 10^{-4} \cdot T + 8.52 \cdot 10^{-8} \cdot T^2 \quad (7)$$

4. PC viscosity is considered constant and equal to $1.112 \cdot 10^{-3}$ kg/ms [19];
5. Fluid thermal expansion coefficient is required by the Boussinesq approximation. The value adopted in the analyses ($\alpha = 1.05 \cdot 10^{-3}$ K^{-1}) has been derived by density measurements at different temperatures [20].

As far as water properties are concerned, the default values provided by ANSYS-Fluent are considered in the present simulations.

4.5 Boundary and initial conditions

The boundary conditions as well as the initial temperature profiles of the calculations have been defined according with the measured temperatures inside the Borexino detector. The *2D water ring* domain, described in Section 4.1, is used to calculate the temperature pattern inside the detector, starting from the LTPS-measured temperatures inside the water tank (ReW) as boundary conditions. The calculated temperatures at the IV surface in this model are subsequently adopted as boundary conditions by the domain, representing the *IV sphere*.

In particular, the boundary temperatures of the *2D water ring* model have been prescribed according to the 14 ReW sensors, which are located approximatively at 50 cm from the stainless steel sphere surface inside the water tank. The boundary profiles have been defined by a linear interpolation of the measured values as a function of both the vertical position and time. On the other hand, the initial temperature profile is prescribed according to a bilinear interpolation procedure as described in [11]. The *2D water ring* initial and boundary temperatures corresponding to October 2018 are given in Figure 8.

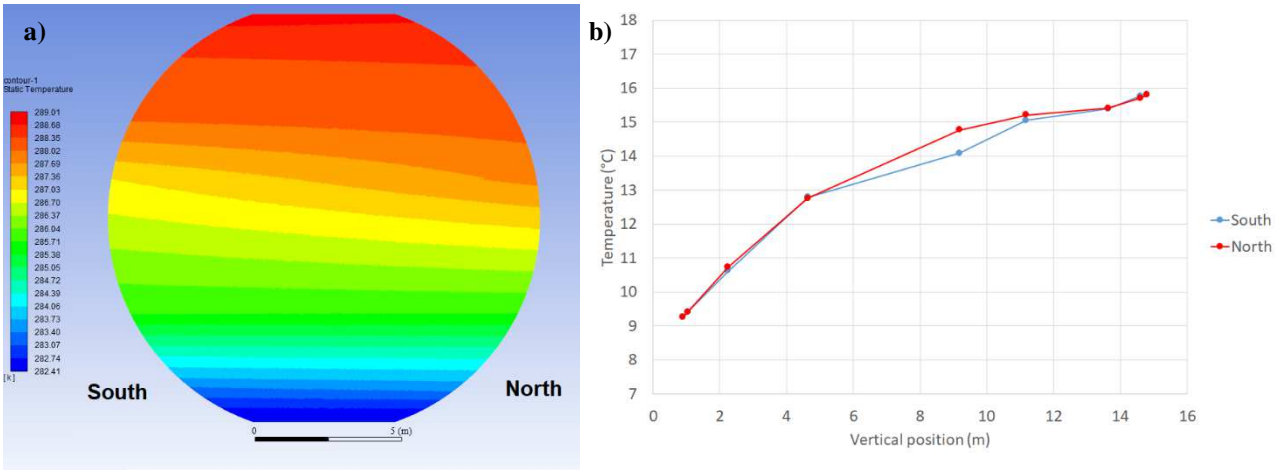

Figure 8: Initial temperature map (a) and vertical temperature profile (b) for the *2D water ring* case (vertical position from the Hall C floor) (colour on-line).

The prescription of the boundary conditions of the *IV sphere* model are essentially based on the same approximate procedure as above. In particular, the calculated temperatures by the *2D water ring* model at the IV surface are sampled at 15 different vertical locations from each side of the inner vessel and then interpolated as described above (see Figure 9).

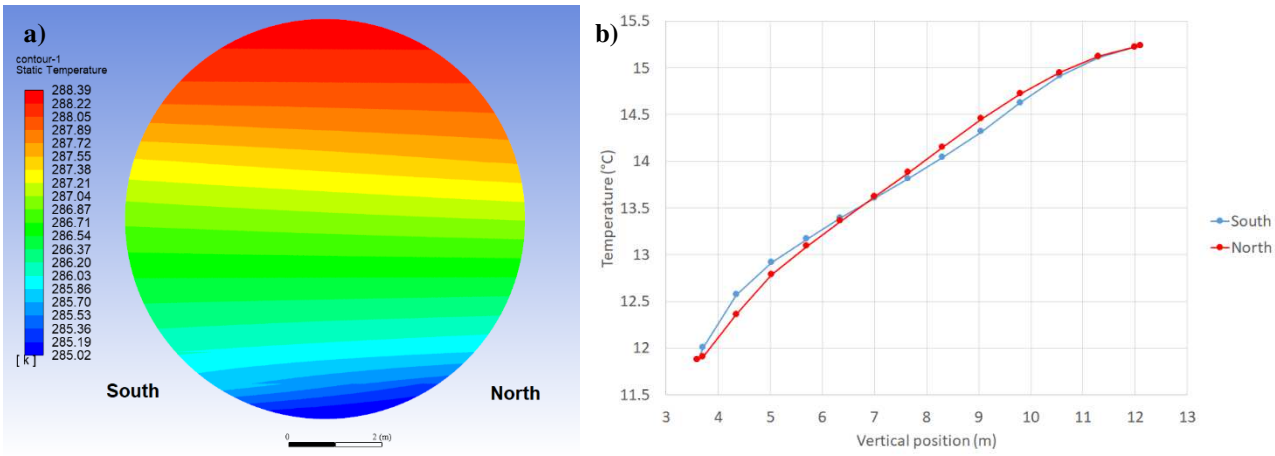

Figure 9: Initial temperature map (a) and vertical temperature profile (b) for the *IV Sphere* case (vertical position from the Hall C floor) (colour on-line).

5. Validation of the CFD model

Several benchmarks focusing on different operating conditions and regimes were carried out in the previous study to verify code compliance and numerical set-up with the typical Borexino convective regimes [11]. In the present section, the validation analysis refers to the developed model described in the section 3, in particular concerning the verification of the temperature prediction capabilities of the *2D water ring* model. Given the remarkable temperature stabilization reached during the past few years, the choice of a recent transient period would not allow to either appreciate or precisely evaluate the time response of the detector (relevant for the verification of the present calculations), due to extremely slow temperature variations. Therefore, the benchmark was carried out considering the Borexino behaviour during 2015, i.e., before the thermal insulation of the detector, since this period is featured by significant temperature oscillations.

The comparison between calculated and measured temperatures (ReB sensors) is presented in Figure 10, along with the temperature residuals in Figure 11. A good agreement can be seen for all the vertical positions, where the numerical code is able to reproduce the temperature evolution of the detector in the selected period. The residuals (simulated temperatures minus measured temperatures) for the 14 ReB probes show also a remarkable accuracy of the present calculations. The discrepancies are larger for the bottom probes N6 and S6 (~ 0.3°C) due to the recirculation pump in the water tank that is not taken into account in the numerical model. After the pump shut-down, however, residuals significantly decrease, showing a better accuracy for almost all the probes (~ ±0.1 °C), comparable with the sensors resolution. Only N7 residual deviates with respect to the others probably due to a non-uniform heat transfer with the rock that may mostly interfere with the bottom sensors.

As far as the time evolution is concerned, a slight temporal phase shift is evident especially when focusing on the top sensors, and appears to be constant, except for small discrepancies in slope change. The cause for this effect might be due to the model discretization and approximation of the initial conditions, but this difference between predicted and measured temperatures is not affecting the overall reliability of the thermal transport benchmarking of this model, being only slightly shifted by a negligible value compared to the simulated period.

In fact, the *2D water ring* model is able to replicate the temperature evolution in the OB (ReB probes), and can be considered a useful tool to understand, replicate and foresee the thermal environment in the

detector. Moreover, it is reasonable to assume that this reliability will hold, for the same geometry, at other points in the model. However, the results presented in this section cannot be considered a fluid transport benchmark, since there is no fluid flow data from Borexino.

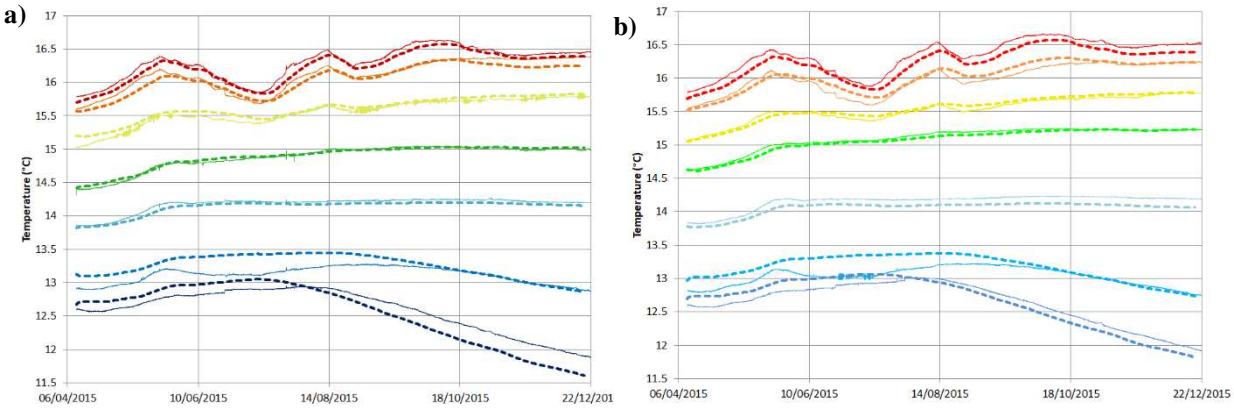

Figure 10: Comparison between measured (full lines) and calculated (dashed lines) temperatures in the south (a) and north (b) side of the detector at the ReB position (colour on-line).

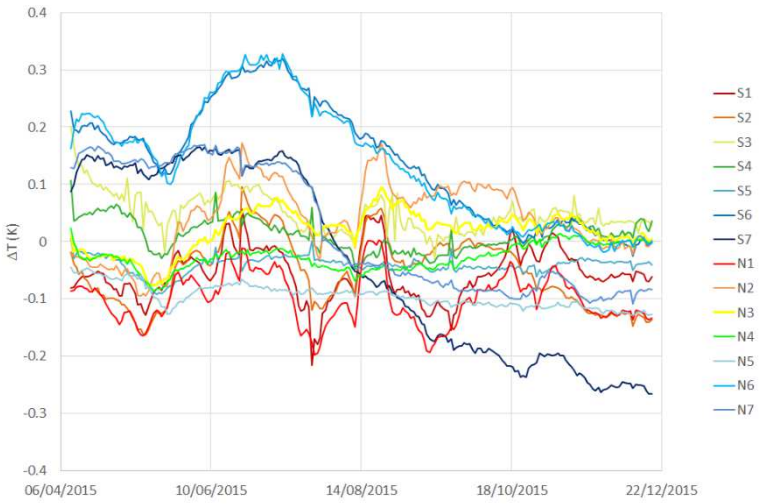

Figure 11: Residuals showing the difference between the simulated and the measured temperatures for the ReB probes. Noticing that divergence of the blue curves is mainly due to the recirculation pump active in the WT (colour on-line).

6. Inner vessel convective currents

In this section the results obtained by the *IV sphere* model simulations are reported. This refined model of the inner vessel volume has been developed to provide a detailed analysis of the velocity field of the scintillator and eventually to explain the behaviour of the ^{210}Po spatial distribution.

Different periods of the Borexino LTPS data are shown in the present section, in order to investigate the relative difference of convective currents inside the detector, which are the responsible for polonium migration. Since the installation of the TIS, polonium levels have significantly decreased due to the mitigation of the convective currents. Nevertheless, an increasing trend during winter, followed by a decrease in summer, can be observed as already shown in Figure 3. This behaviour is better depicted in Figure 12, where polonium oscillations, which dominates the bottom part of the fiducial volume, seem to be strongly correlated with the vertical temperature gradient. Therefore, the seasonal periods summer/winter 2017 and 2018 have been selected for the analyses:

- "Feb2017": 21.01.2017 – 20.02.2017
- "AugSep2017": 01.08.2017 – 13.09.2017
- "Apr2018": 01.04.2018 – 30.04.2018
- "Oct2018": 01.10.2018 – 30.10.2018

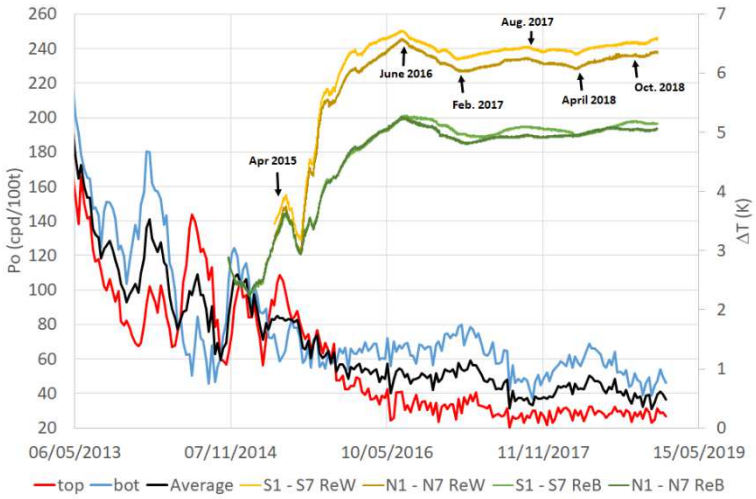

Figure 12: ^{210}Po rate in the fiducial volume (r < 2.5 m and |z| < 1.5 m) compared with the detector temperature gradient (colour on-line).

As far as the temperature is concerned, the typical inner vessel map and the relative isotherms are depicted in Figure 13. The calculated profiles show the thermal stratification of the detector that is featured by well-defined horizontal isotherms across the inner vessel volume. However, the very proximity of inner vessel surface is characterized by a steep temperature gradient which is directly determined by the longitudinal temperature asymmetry (see Figure 9b), and can significantly affect the fluid buoyancy term and thus, the convection in this narrow region.

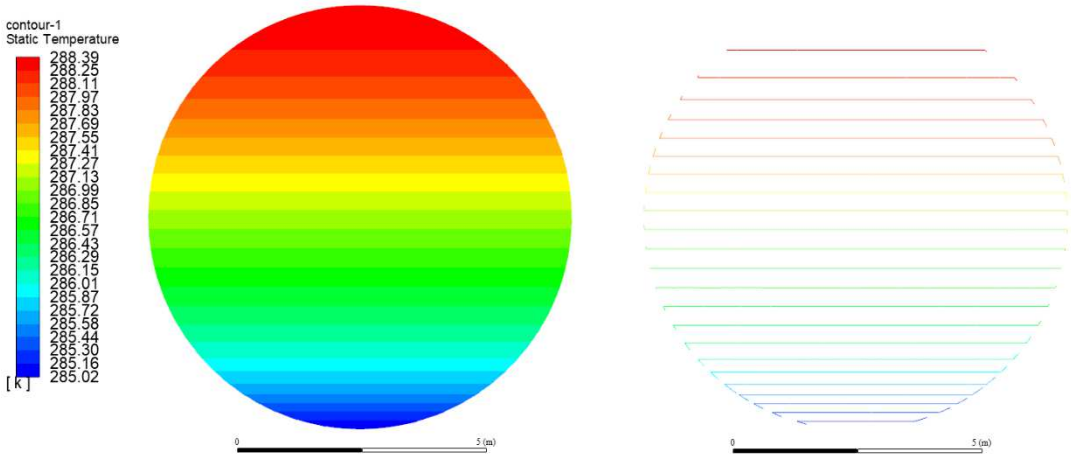

Figure 13: Typical temperature map (left) and isotherms (right) of the Borexino IV. Note that the "steep temperature gradient" referenced in the text above is visible in the right plot as spikes at the boundary.

This temperature pattern implies a peculiar fluid-dynamics behaviour of Borexino as illustrated by the stream function [14] map (representing the fluid carrying capacity of the flow) and the velocity magnitude vectors, depicted in Figure 14 and Figure 15, respectively, and only shown here for a particular 1-month period of 2018 (named as reference period in the following), for the sake of brevity. The stream function φ is defined by eq. (8), where u_x and u_y are the velocity vector components. φ is constant along a streamline (i.e., the tangent line to the velocity vector) and the difference between constant values of stream function is the mass rate of flow between the streamlines. The results show that horizontal currents are the dominant feature in the domain, as indicated by the stream lines as well as by the velocity vectors. Indeed, the large buoyancy potential energy gap between the top and bottom, separating the stably-stratified fluid layers, precludes bulk, organized motion in the IV. For a given vertical gradient, temperature asymmetries between both sides affect the intensities of such currents, that transport fluid from one side of the sphere to the other one, while leaving the stratification in place.

$$\rho u_x \equiv \frac{\partial \varphi}{\partial y}; \qquad \rho u_y \equiv \frac{\partial \varphi}{\partial x} \tag{8}$$

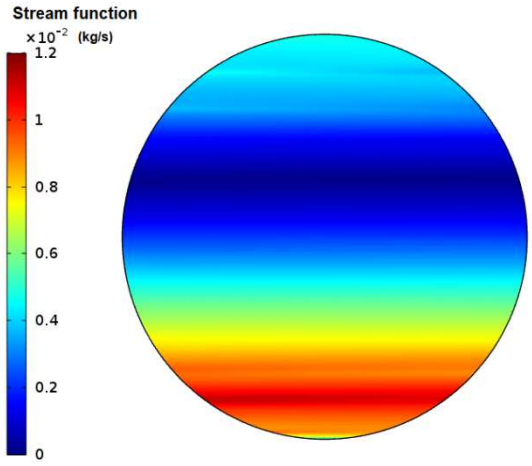

Figure 14: Typical stream function map of the Borexino IV (colour on-line).

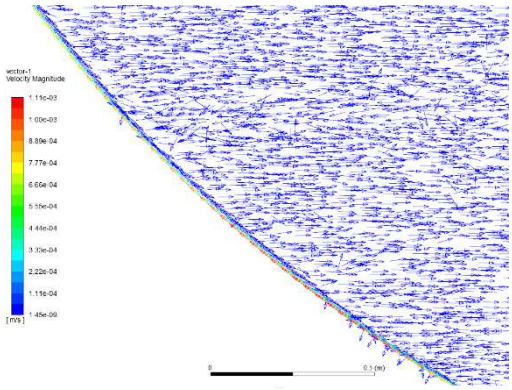

Figure 15: Velocity vectors map of the lower portion of the IV coloured with the velocity magnitude intensity (colour on-line).

Furthermore, the vicinity of the IV surface is characterized by strong vertical currents up to ~3 orders of magnitude larger than those in the bulk of the IV. Such currents are directly induced by the steep temperature variations at boundary (Figure 13). In particular, in the bottom part, the left side (south) shows a current directed upwards (hotter side) whereas the right side shows a downward flow. The situation is opposite in the upper part of the vessel since the temperatures are inverted between left and right. This behaviour, even if very localized, might affect the ^{210}Po transport since it is supposed to originate from the less radio-pure vessel nylon and to migrate into the FV scintillator.

As far as the interior currents are concerned, the horizontal velocities are of the order of 10^{-7}-10^{-6} m/s (Figure 16). The order of magnitude of these (organized) currents is extremely relevant to the ^{210}Bi-^{210}Po equilibrium in Borexino.

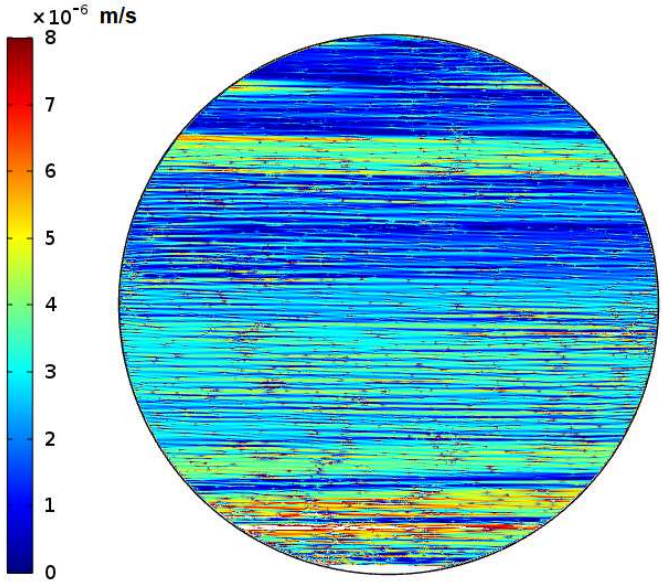

Figure 16: Horizontal velocity magnitude $|v_x|$ in the Borexino IV (colour on-line).

A 1 µm/s horizontal scintillator flow directed away from the vessel (neglecting probable small-scale recirculation at the vessel surface currents or in small-scale vortices in the bulk) means that it will take at least ~18 days for that fluid to reach the FV. It must be mentioned that the contribution of the diffusion to the ^{210}Po transport is very small compared to convection: since the diffusion length is about 13.1 cm [21], it is substantially impossible for ^{210}Po to reach the FV by diffusion mechanism only. This convective time scale (18 days) constitutes >3 half-lives for ^{210}Bi, and will typically be longer for realistic flow paths and locations away from the FV boundary. ^{210}Bi concentrations will therefore be stable everywhere in the FV and mostly unaffected by peripheral contamination from the vessel, as long as this approximate regime is kept below ~5 µm/s. At the same time however, these conditions ensure a large part of the ^{210}Po born from ^{210}Bi decay will still travel deep inside the FV before decaying, and even be able to recirculate twice inside the IV within a single half-life of 138 days. Effectively, this suggests layers of approximately-constant, out-of-equilibrium concentrations of ^{210}Po bounded by the vertical thickness of such horizontal regions, down to very weak fluid velocities ~$5 \cdot 10^{-8}$ m/s, or slightly above considering realistic recirculation effects. The system thus would be located at an intermediate point in the relationship between fluid dynamic stability and radio-background concentration, where ^{210}Bi stability is assured even in areas with relatively elevated flow speeds, while ^{210}Po will generally exhibit vertical (but not horizontal) regional variations, seemingly exacerbated by increasing isotherm slope (that is, side-to-

side temperature asymmetries). These early qualitative interpretations will be further explored in the following section.

From the stream function as well as from the horizontal currents maps, 3 main regions can be identified: the very top part, that is featured by average-intensity flow currents; a middle-top region where the flow is very small compared to the rest of the domain; and a middle-bottom region characterized by stronger convective currents.

This behaviour can be better appreciated by the stream function vertical profiles in the middle of the inner vessel, shown in Figure 17, for the different analysed periods. From the qualitative point of view, the results show that there is a region of minimal flow currents that actually agrees with the polonium concentration measurements inferred from Borexino data, whereas the bottom part of the IV is affected by significant transport. However, if we consider that polonium is mainly brought into the fiducial volume from the vessel surface, the stream function cannot qualitatively describe its behaviour, and, therefore a detailed transport model is required for a better understanding and simulation of the polonium migration inside Borexino (see next section).

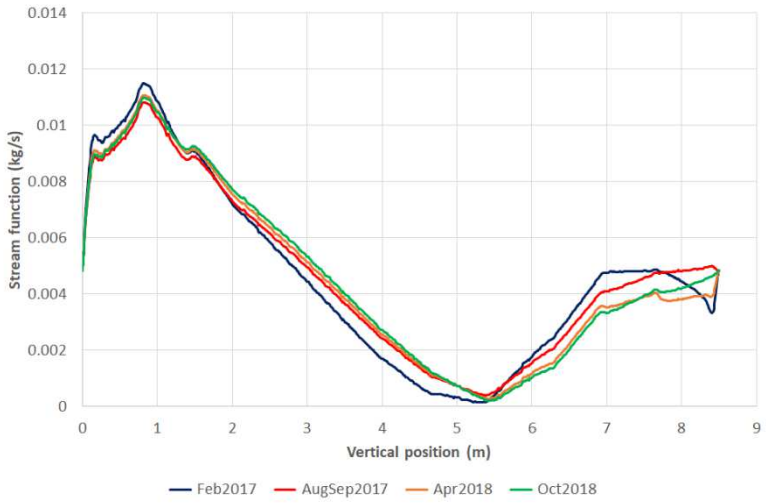

Figure 17: Stream function vertical profiles for the different analysed periods (colour on-line).

7. Transport modelling and Po predictions

In order to investigate the polonium migration inside the inner vessel a simplified transport model has been developed.

Since there is no experimental evidence indicating that ^{210}Bi and ^{210}Pb are able to migrate inside the inner vessel from the nylon sphere, they do not need to be treated in the present analysis. Although this hypothesis is still under discussion, they are assumed to be completely mixed inside the IV volume with a uniform concentration. In fact, the main chain progenitor ^{210}Pb ($t_{1/2}$ = 22.3 y) constitutes an "inexhaustible" (from the point of view of detector operations) source of ^{210}Bi/Po, and would impede reaching a baseline equilibrium level of ^{210}Po if mobile, for any physical flow speed. However, it is clear this is not the case from the past out-of-equilibrium ^{210}Po decay events, and ^{210}Pb can be considered to be adsorbed on the vessel nylon material. This hypothesis is also strengthened by knowledge gained during the fabrication of Borexino's vessels and their chemical analysis. This means ^{210}Pb can be safely ignored in the migration simulation. On the other hand, polonium is extremely mobile and can diffuse through the nylon sphere being transported inside the vessel by convective currents [21][22].

In order to model the transport phenomenon described above the convection-diffusion equation is considered for ^{210}Po only, as follows:

$$\frac{\partial c_{Po}}{\partial t} + \nabla \cdot (-D\nabla c_{Po}) + \mathbf{u}\nabla c_{Po} = -\lambda_{Po} c_{Po} \quad (9)$$

where c_{Po} is the Po concentration, D the diffusion coefficient (~ 10^{-9} m^2/s), **u** the fluid velocity vector and λ_{Po} the Po decay constant. The transport equation has been solved by means of the finite-element commercial software COMSOL Multiphysics [23], adopting the same spatial discretization of the Fluent CFD calculations.

As far as the boundary condition to the above equation is concerned, the ^{210}Po concentration at the IV surface is assumed to be uniform and constant. The velocity field is taken from the CFD solution described in the previous section, assuming a constant velocity map over time for each considered period of interest. This is a reasonable approximation as demonstrated by the CFD analyses, and it allows to greatly simplify the numerical burden by decoupling the CFD problem from the transport analysis.

The typical calculated ^{210}Po activity (stationary solution) is reported in Figure 18, whereas the comparison with the measured rates is reported in Figure 10 and Figure 11 for the analysed periods. In

addition, a control case with a perfect side-to-side stratification (horizontal isotherms) has been developed in order to check the transport mechanism in a case where little convection should occur.

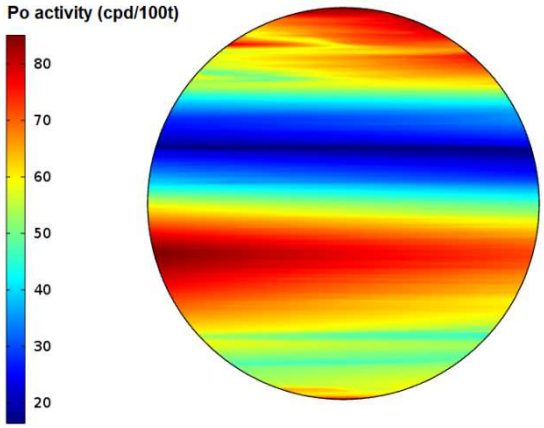

Figure 18: Calculated ^{210}Po activity in the inner vessel for the reference period (colour on-line).

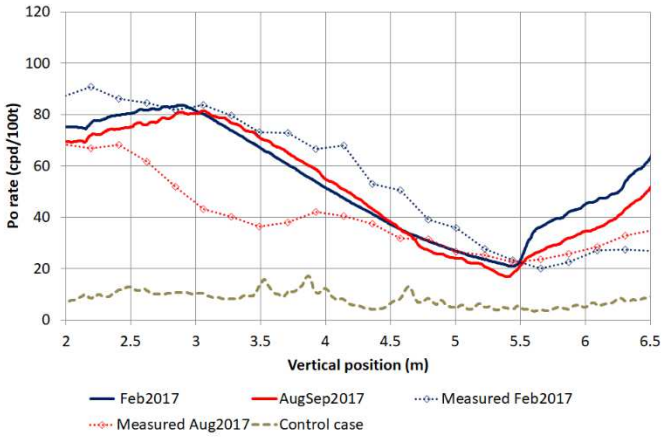

Figure 19: Calculated vs. measured Po rate along the IV vertical position (from the IV bottom) inside a r < 2.25 m FV during "Feb2017" and "AugSep2017" periods (colour on-line).

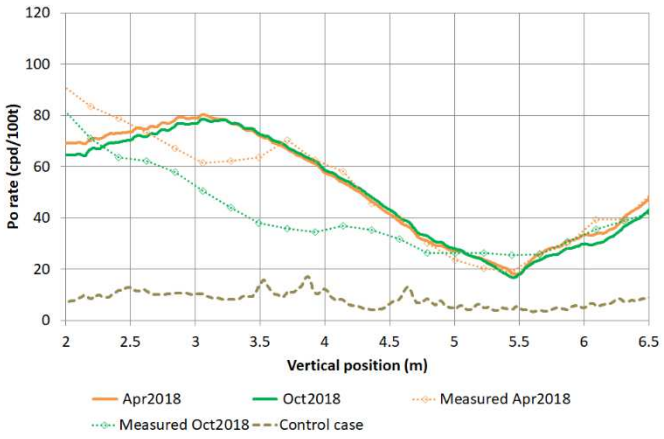

Figure 20: Calculated vs. measured Po rate along the IV vertical position (from the IV bottom) inside a r < 2.25 m FV during "Apr2018" and "Oct2018" periods (colour on-line).

Results clearly indicate that the temperature-induced convective currents produce a region of lower ^{210}Po concentration consistently with experimental findings. Such currents are mainly driven by the north-south temperature asymmetries, characteristic of Borexino Hall C environment. This is indicated by the very low polonium activity calculated in the control case of equal north-south temperatures at the same height levels.

The agreement with the experimental data is very good concerning the winter periods (especially for "Apr2018") and for the top part of the fiducial volume. However, the calculated concentration presents some discrepancies compared with the measured data. In particular, the ^{210}Po concentration is underestimated at the very bottom FV, whereas it shows a slight overestimation at the top part for the 2017 periods. In addition, the seasonal variations are not well reproduced by the calculations, showing an overestimation of the ^{210}Po activity for both the summer periods. Such discrepancies are probably due to the temperature boundary conditions imposed to the CFD analysis. Despite the general good agreement shown in Figure 10, the temperature profile over the whole IV height is approximated by only 3 point-like measurements of the corresponding LTPS sensors available for that region, which induces a large interpolation uncertainty. Moreover, there is also a large uncertainty in the position of some of the probes (S1, S2, S4, S6), since it was never accurately measured in the past, therefore increasing the uncertainty on the overall temperature profile of the inner vessel. A possible way to reduce this uncertainty would involve an external calibration like that performed in 2011-12 [9] - at that time, some re-entrant tube positions were left unused since precision determination of all tubes was not a requirement.

With the above caveats, the results presented in this section provide important indications about the ^{210}Po behaviour and indicate that ^{210}Po concentration asymmetries between the top and the bottom of the fiducial volume are mainly determined by the convective pattern inside the detector IV.

8. Conclusions

This paper investigated the fluid dynamics behaviour of the Borexino neutrino detector and the polonium background transport phenomenon by means of detailed CFD analyses. Two combined models have been developed in order to obtain a satisfactory accuracy in the velocity pattern results. Due to the nature of the convective currents and the size of the detector, the computational requirements are significant. The *2D water ring* model, that was adopted to perform the thermal analysis, is in a very good agreement with the measured temperatures inside the detector, thereby further strengthening a working, precise thermal transport model. The calculated temperatures are applied as boundary conditions to the inner vessel model which is adopted to calculate the flow field. The results indicate that the convective currents mainly develop horizontally and are basically driven by the temperature difference between the north and the south side of the IV due to the stratified structure of the flow. The stream function profiles are qualitatively in agreement with the measured polonium concentration, but a detailed transport analysis is required to analyse the ^{210}Po convection. To this purpose, a transport model has been specifically developed in which the IV velocity map is imported from the CFD calculations. The results are very promising showing a general good agreement between measured and calculated ^{210}Po activity in the fiducial volume. However, some discrepancies have been encountered such as the fact that the model is not able to reproduce the seasonal ^{210}Po variation in the FV bottom, that are likely due to the uncertainties on the temperature boundary conditions. In order to improve the current status, a more accurate temperature profile is required. A full 3D CFD model of the IV is also being developed in order to gain a better understanding of the convective currents, considering eventual azimuthal effects. These simulations are fundamental for the comprehension of the general fluid-dynamics inside Borexino as well as for the final CNO strategy.

Acknowledgment

The Borexino program is made possible by funding from INFN (Italy), NSF (USA), BMBF, DFG, HGF and MPG (Germany), RFBR (Grants 16-02- 1570 01026 A, 15-02-02117 A, 16-29-13014 ofi-m, 17-02-00305 A) (Russia), and NCN Poland (Grant No. UMO-2013/10/E/ST2/00180). The authors wish to acknowledge the precious support of the Politecnico di Milano (Italy) where most of the numerical simulations in this study have been performed thanks to the availability of HPC system of the interdepartmental laboratory 'CFDHub'.

References

[1] Borexino Collaboration, Comprehensive measurements of pp-chain solar neutrinos, Nature 562 (2018) 505-510. https://doi.org/10.1038/s41586-018-0624-y.

[2] Borexino Collaboration, Neutrinos from the primary proton-proton fusion process in the Sun, Nature 512 (2014) 383-386. https://doi.org/10.1038/nature13702.

[3] Borexino Collaboration, First evidence of pep solar neutrinos by direct detection in Borexino, Phys. Rev. Lett. 108 (2012) 051302. https://doi.org/10.1103/PhysRevLett.108.051302.

[4] Borexino Collaboration, Precision measurement of the ^{7}Be solar neutrino interaction rate in Borexino, Phys. Rev. Lett. 107 (2011) 141302. https://doi.org/10.1103/PhysRevLett.107.141302.

[5] Borexino Collaboration, Measurement of the solar ^{8}B neutrino rate with a liquid scintillator target and 3 MeV energy threshold in the Borexino detector, Phys. Rev. D 82 (2010) 033006. https://doi.org/10.1103/PhysRevD.82.033006.

[6] Borexino Collaboration, Spectroscopy of geo-neutrinos from 2056 days of Borexino data, Phys. Rev. D 92 (2015) 031101. https://doi.org/10.1103/PhysRevD.92.031101.

[7] Borexino Collaboration, Comprehensive geoneutrino analysis with Borexino, submitted to Physical Review D. arXiv:1909.02257 [hep-ex].

[8] J. Benziger, The Borexino purification system, Int. J. Mod. Phys. A 29 (2014) 1442002.

[9] Borexino Collaboration, Borexino calibrations: Hardware, Methods, and Results, JINST 7 (2012) P10018.

[10] Isover Saint-Gobain, U Tech Roll 2.0 datasheet. https://www.isover.it/download/scheda-tecnica-u-tech-roll-20, 2015.

[11] D. Bravo-Berguño, R. Mereu, P. Cavalcante, M. Carlini, A. Ianni, A. Goretti, F. Gabriele, T. Wright, Z. Yokley, R.B. Vogelaar, F. Calaprice, F. Inzoli, The Borexino Thermal Monitoring & Management System and simulations of the fluid-dynamics of the Borexino detector under asymmetrical, changing boundary conditions, Nucl. Instrum. Meth. A 885 (2017) 38-53. https://doi.org/10.1016/j.nima.2017.12.047.

[12] N. Vinyoles, A. M. Serenelli, F. L. Villante, S. Basu, J. Bergström, M. C. Gonzalez-Garcia, M. Maltoni, C. Peña-Garay, N. Song, A New Generation of Standard Solar Models, ApJ 835 (2017) 202. doi:10.3847/1538-4357/835/2/202.

[13] F.L. Villante, A. Ianni, F.Lombardi, G. Pagliaroli, F. Vissani, A step toward CNO solar neutrino detection in liquid scintillators, Phys. Rev. B 701 (2011) 336-341. https://doi.org/10.1016/j.physletb.2011.05.068.

[14] ANSYS Fluent User's Guide, ANSYS, Inc., 275 Technology Drive Canonsburg, PA 15317, November 2010.

[15] W. Malalasekera, H. K. Versteeg, An Introduction to Computational Fluid Dynamics: The Finite Volume Method, Prentice Hall, 2007.

[16] 1,2,4-Trimethylbenzene, Pseudocumene properties. http://www.microkat.gr/msdspd90-99/1%2C2%2C4-Trimethylbenzene.html.

[17] W. E. Putnam, J. E. Kilpatrick, Entropy, Heat Capacity, and Heats of Transition of 1,2,4-Trimethylbenzene, J. Chem. Phys. 25 (1957) 1075-1080.

[18] G. Latini, G. Di Nicola, M. Pierantozzi, A Critical Survey of Thermal Conductivity Literature Data for Organic Compounds at Atmospheric Pressure and an Equation for Aromatic Compounds, Energy Procedia 45 (2014) 616-625.

[19] Matweb, Material property data, 1,2,4-Trimethylbenzene. http://www.matweb.com/search/DataSheet.aspx?MatGUID=bbf5c47699b5499dbfaa20c3eba1b4b8&ckck=1.

[20] PubChem, 1,2,4-Trimethylbenzene. https://pubchem.ncbi.nlm.nih.gov/compound/1_2_4-trimethylbenzene.

[21] M. Misiaszek, K. Pelczar, M. Wójcik, G. Zuzel, M. Laubenstein. Optimization of low-background alpha spectrometers for analysis of thick samples, Appl. Radiat. Isot. 81 (2013) 146-150. https://doi.org/10.1016/j.apradiso.2013.03.006.

[22] M. Wójcika, W. Wlazło, G. Zuzel, G. Heusser, Radon diffusion through polymer membranes used in the solar neutrino experiment Borexino, Nucl. Instrum. Meth. A 449 (2000) 158-171. https://doi.org/10.1016/S0168-9002(99)01450-3.

[23] Comsol Multiphysics® V. 5.4, www.comsol.com, COMSOL AB, Stockholm, Sweden.